IOP Publishing Journal of Physics: Condensed Matter
J. Phys.: Condens. Matter **29** (2017) 035002 (12pp) doi:10.1088/0953-8984/29/3/035002

Assessing the amorphousness and periodicity of common domain boundaries in silica bilayers on Ru(0001)

Kristen M Burson[1,2], Christin Büchner[1], Markus Heyde[1] and Hans-Joachim Freund[1]

[1] Fritz-Haber-Institute of the Max-Planck-Gesellschaft, Faradayweg 4-6, 14195 Berlin, Germany
[2] Department of Physics, Hamilton College, Clinton, NY 13323, USA

E-mail: heyde@fhi-berlin.mpg.de

Received 28 July 2016, revised 13 October 2016
Accepted for publication 25 October 2016
Published 15 November 2016

Abstract

Domain boundaries are hypothesized to play a role in the crystalline to amorphous transition. Here we examine domain boundary structures in comparison to crystalline and amorphous structures in bilayer silica grown on Ru(0001). Atomically resolved scanning probe microscopy data of boundaries in crystalline bilayer films are analyzed to determine structural motifs. A rich variety of boundary structures including rotational, closed-loop, antiphase, and complex boundaries are identified. Repeating units with ring sizes of 558 and 57 form the two most common domain boundary types. Quantitative metrics are utilized to assess the structural composition and degree of order for the chemically equivalent crystalline, domain boundary, and amorphous structures. It is found that domain boundaries in the crystalline phase show similarities to the amorphous phase in their ring statistics and, in some cases, in terms of the observed ring neighborhoods. However, by assessing order and periodicity, domain boundaries are shown to be distinct from the glassy state. The role of the Ru(0001) substrate in influencing grain boundary structure is also discussed.

Keywords: silica, crystalline, amorphous, domain boundaries, 2D material, scanning tunneling microscopy

(Some figures may appear in colour only in the online journal)

1. Introduction

Domain boundaries and defect structures are determining factors for materials strength, electronic behavior, and chemistry. They also can provide insight into the relationship between crystalline and glassy materials. The structure of the glass transition remains a topic of active debate and it is hypothesized that domain boundaries (also called grain boundaries) are structurally similar to glassy states. It has also been suggested that amorphous materials may be described as crystalline materials with a large number of domain boundaries. For example, one early prediction, the crystallite theory, proposed that amorphous materials consist of many small silica crystals (crystallites) interconnected by domain boundaries. Crystallites were presumed to rigidly maintain a silica crystal structure. However, this early theory was inconsistent with numerous x-ray and neutron diffraction experiments that have since been performed on the model glass former silica [1, 2]. A more modern version of that theory posits that 'cybotactic groupings', small clusters of ordered atomic groups which are crystalline-like with distortions, are frozen-in to the vitreous state as it is quenched [3, 4]. In this theory, the vitreous phase is nanoheterogeneous. Another prediction about the relationship between domain boundaries and amorphous structures addresses bulk polycrystalline materials. The Rosenhain 'amorphous cement' model proposes that amorphous grain junctions 'cement' together microcrystalline domains [5]; the theory is supported by several molecular dynamics simulation studies of domain boundaries [6, 7]. For crystalline SiO_2 structures, it has been found that vitrification nucleates at domain boundaries [8, 9]. In order to address the relationship between domain boundaries and amorphous phases,

comparisons must be made between chemically equivalent systems which exhibit both crystalline and amorphous forms. 2D materials are a promising candidate for these comparisons because they can be readily studied with atomic-scale spatial resolution using surface science techniques.

In addition to providing insight into the glass transition, domain boundaries are important because they affect material properties. For 2D materials, domain boundaries have an important impact on mechanical and electronic properties [10–12]. For example, experimental evidence shows that the mechanical strength of graphene is weakened by the presence of domain boundaries [13]. Straight 1D defect structures may be engineered as a metallic wire in graphene [14] and grain boundary loops in graphene have been investigated for similar effects [15]. Domain boundaries are equally significant in other 2D materials, such as the transition metal dichalcogenides [16–18]. The presence of varying pore sizes in the atomic structure introduced by domain boundaries and defects can have an important effect on the chemical properties of the system; for example, in 2D silica samples with both crystalline and vitreous regions, Pd atoms can be adsorbed in both crystalline and vitreous patches while Au atoms selectively adsorb only in vitreous regions [19]. This difference is attributed to the presence of larger pores in the vitreous regions, which are required for penetration of the larger Au atoms into the silica layer. For monolayer silica structures on Mo(1 1 2), 1D defects have similarly been shown to function as atomic sieves [20, 21]. The field of domain boundary engineering seeks to utilize the influence of domain boundaries for tailoring electronic devices, catalytic materials, and other technologies [22]. Understanding the nature of domain boundary structures is of particular importance for domain boundary engineering.

2D model silica structures are ideal systems for addressing the similarities between experimentally observed defects in crystalline domains and the hypotheses of the various models previously discussed. Studies have reported observations of domain boundary and defect structures in monolayer (ML) and bilayer (BL) silica grown on various substrates (summarized in table 1); these results point to the utility of the silica material system for addressing domain boundaries in particular. Furthermore, the atomic structure of bilayer silica has been determined for both crystalline and amorphous film preparations. Amorphous and crystalline preparations of silica exhibit the same chemical composition and basic structural building blocks, corner-connected SiO_4 tetrahedra, but differ in arrangement of these building blocks. Specifically, the amorphous structures exhibit a greater distribution in the O–Si–O bond angle which determines positions of adjacent SiO_4 units [32]. As a result, long-range periodicity is not observed. The atomically flat nature of 2D bilayer silica makes the structures ideally suited for characterization with surface science techniques. Real-space atomic position data of bilayer silica structures from low-temperature scanning probe microscopy measurements and transmission electron microscopy experiments has been presented and the atomic scale and neighborhood structures of the rings have previously been analyzed [24, 32–37]. These earlier studies present a clear metric for the nature of amorphous structures in 2D silica films from which structural similarities between the amorphous silica and domain boundaries and defects can be determined.

Here we present a low temperature scanning tunneling microscopy study of common domain boundaries and defects observed within crystalline configurations of bilayer silica on Ru(0 0 0 1). Multiple metrics are presented to describe their relationship to amorphous silica structures. Furthermore, the relationship between common domain boundaries and the underlying Ru(0 0 0 1) substrate is discussed.

2. Methods

Bilayer silica films were grown on Ru(0 0 0 1) substrates in an ultra-high vacuum chamber equipped with low energy electron diffraction (LEED), Auger electron spectroscopy (AES), and a scanning probe microscope. Ru substrates were first treated with cycles of Ar^+ sputtering and UHV annealing and examined with LEED, AES, and STM to control cleanliness prior to sample growth. Well-defined bilayer SiO_2 structures were grown by evaporating silicon onto preoxidized 3O-(2 × 2)/Ru(0 0 0 1) at $T = 300\,K$ and subsequently annealing to $T \approx 1200\,K$ in the presence of 2×10^{-6} mbar O_2. Samples were cooled in the oxygen environment. Sample preparation yields either vitreous or crystalline configurations, which may depend on the coverage and the rate of cooling [32, 38]. Coverage is expressed in terms of monolayers (MLs), where 2MLs are equivalent to a fully closed bilayer. We observe more crystalline areas with higher coverages (1.9–2.0 MLs), while coverages between 1.5–1.8 MLs yield larger amorphous domains. All samples considered in this study contained crystalline regions. Topographic images were attained using a custom-built, low temperature (4 K) STM with a PtIr tip [39, 40].

3. Silica structures: comparing crystalline, domain boundary, and amorphous structures

All bilayer silica structures, whether amorphous, crystalline, or domain boundaries, are composed of tetrahedral SiO_4 building units; adjacent tetrahedra share an oxygen. Looking at the flat top layer of the silica, a network of ring structures can be observed, such as those shown in the STM images in the left-hand column of figure 1. Oxygen bridges connect two equivalent planes of the silica ring structures to form bilayer silica. As such, the bonding structure of the silica is completely self-saturated and there is only a weak van der Waals interaction between the silica structure and the underlying Ru(0 0 0 1) substrate. Coordination defects, vacancies, and charge traps are not observed. Here we will focus on structural defects, specifically considering non-crystalline structural features within crystalline domains that result from flexibility in the connection angles of the SiO_4 tetrahedra. Previous studies have examined the ring size distributions in crystalline and amorphous silica [32, 35, 41]. Here, ring size is defined by the number of silicon atoms contained in a particular ring. Ring sizes are determined directly from the topographic images by

Table 1. Summary of boundaries and defect structures identified in monolayer (ML) and bilayer (BL) silica grown on various substrates as well as in bulk silica. Scanning tunneling microscopy (STM), atomic force microscopy (AFM), helium atom scattering (HAS), density functional theory (DFT) and classical force field (CFF) approaches have been used in the literature to investigate domain boundary structures.

System	Boundaries and common defects	Method	Citation
BL SiO_2/Ru(0001)	• 558 antiphase domain boundary • 57 rotational domain boundary • 48 domain boundary • Stone–Wales defect • 57 closed-loop defects	AFM STM	*current study* Büchner *et al* [19]
BL SiO_2/grapheme	• 57 rotational domain boundary • Stone–Wales defect • 57 closed-loop defects	TEM DFT CFF	Bjorkman *et al* [23]
BL SiO_2/Pd(001)	• Elongated 8MR antiphase boundary	STM	Altman *et al* [24]
BL SiO_2/Pt(111)	• Only amorphous structures observed	STM	Yu *et al* [25]
4 nm SiO_2/Ni(111)	• Antiphase domain boundaries (no atomic resolution)	STM	Kundu *et al* [26]
BL $Al_xSi_{1-x}O_2$/Ru(0001)	• 48 antiphase domain boundary • 5577 domain boundary	STM	Boscoboinik *et al* [27]
ML SiO_2/Mo(112)	• 48 antiphase domain boundary	STM	Weissenrieder *et al* [28] Ulrich *et al* [20]
ML SiO_2/Ru(0001)	• 5577 domain boundary • 57 triangular loop defect encompassing a 6MR • 475 rectangular loop defect encompassing an 8MR	STM	Mathur *et al* [29] Yang *et al* [30]
Bulk silica α-quartz (0001) surface reconstruction	• Dauphiné twin boundary composed of 6MRs	HAS AFM DFT	Eder *et al* [31]

counting the number of atoms in a ring, or in cases where the image resolution limits silicon or oxygen atomic position assignments, ring size can be determined by assessing the number of neighboring rings. An ideal crystalline region consists only of 6-membered rings (figure 1(a)) while amorphous bilayer silica consists primarily of 4–9 membered rings (figure 1(c)). For amorphous silica, a log normal distribution of ring sizes has been observed consistent with theoretical predictions for random 2D networks [36, 42]. More five-membered rings are observed than seven-membered and more eight-membered rings are observed than four-membered rings. Nine-membered and larger rings composed a small portion of the total rings in the amorphous structure.

Crystalline structures with domain boundaries and defects lie somewhere between purely crystalline and amorphous systems; they may be classified as polycrystalline or defected materials. The ring statistics for crystalline structures with domain boundaries are shown in figure 1(b), in comparison with those of purely crystalline (figure 1(a)) and amorphous (figure 1(c)) silica. An extended network of domain boundaries with over 1500 rings was analyzed to develop meaningful ring statistics, shown in figure 1(b) in order to best represent the low-density of defect structures. Like the ideal crystalline silica system, these structures are primarily comprised of six-membered rings. However, they exhibit four- to eight-membered rings showing more five-membered rings than seven-membered rings and more eight-membered rings than four-membered rings, similar to amorphous systems. Nine membered rings, which comprise approximately 1% of the rings present in amorphous silica structures, were not observed in defected crystalline domains. In order to identify similarities between crystalline, domain boundary, and amorphous structures, we will analyze the ring size distributions shown in figure 1.

The ring statistics for defected crystalline structures differ from the log-normal distribution of the amorphous bilayer silica structures. Log-normal ring statistics are characteristic of random network formers [42]. For figure 1(b), the ring statistics are counted for crystalline samples with point and line defects, which typically occur in low densities, and are therefore dominated by six-membered rings from the crystalline domains. In this case, we would not expect log-normal behavior. Would the ring statistics be consistent with those of amorphous structures if the defected crystalline films had higher densities of comparable defects? Answering this question provides insight into whether domain boundaries serve as precursors for the glassy state. To address this question, we model an enhancement of the defect density starting with the ring statistics collected for the defected crystalline domain as presented in figure 1(b). The approach considers the ring statistics of defected crystalline structures with a decrease in the number of six-membered rings while holding the ring counts and proportions of all other ring sizes fixed, hence simulating an increase in defect structure density within crystalline domains. These modified ring statistics serve as one metric for evaluating whether amorphous silica structures could be derived from crystalline silica by introducing a large number of domain boundaries. The 'enhanced domain boundary model' ring statistics are evaluated with a log-normal fitting in order to assess similarities between the model and characteristic amorphous distributions. Reducing the number of six-membered rings by a factor of 6.5 from the

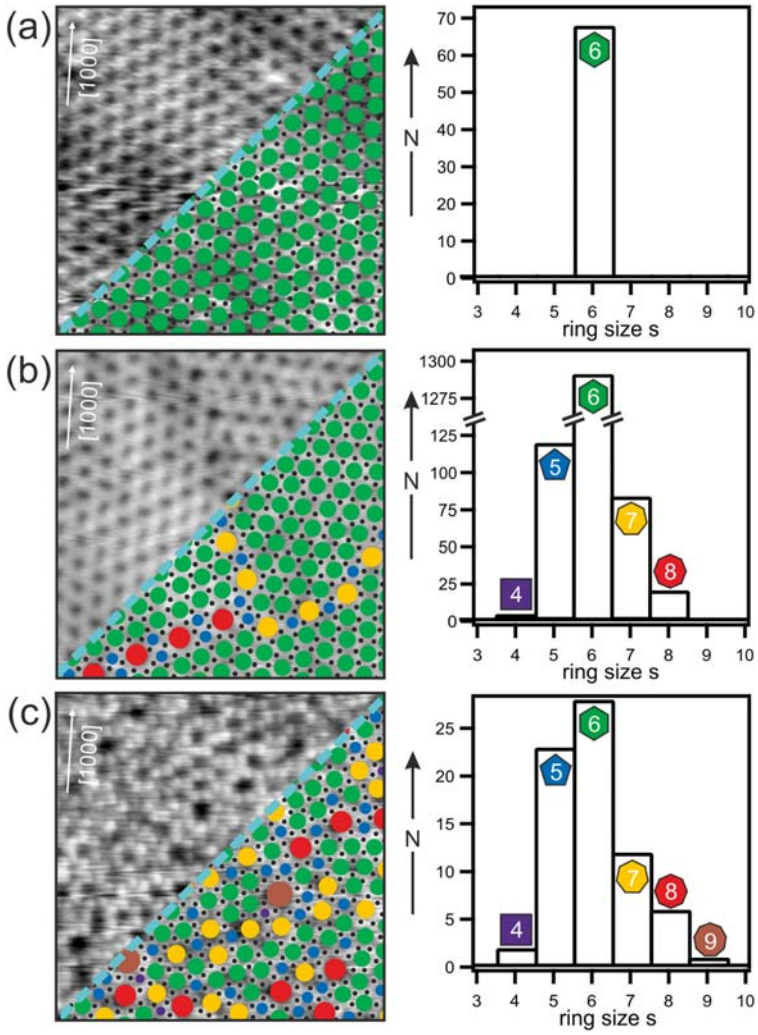

Figure 1. Ring statistics. STM images and ring size distributions for (a) purely crystalline silica (I_T = 100 pA, V_S = 1.0 V, scan area = 7.4 nm × 7.4 nm), (b) crystalline silica with domain boundaries (I_T = 100 pA, V_S = 0.5 V, scan area = 7.4 nm × 7.4 nm), and (c) amorphous silica (I_T = 50 pA, V_S = 2.0 V, scan area = 7.4 nm × 7.4 nm). Silicon atomic positions are identified with black dots and ring sizes are color coded.

statistics in figure 1(b) optimizes the log-normal fit. In this case, a log-normal distribution is attained with fit parameters which are within the range of other known random network formers [43]. This suggests that high structural defect densities in crystalline silica phases are consistent with the global ring distributions in amorphous silica structures, but further metrics are needed which address comparisons of local structures (see section 4).

Ring statistics can also be assessed in the context of the geometric constraints of 2D systems. Euler's theorem predicts the following requirement for the ring-size populations of closed 2D planar structures:

$$\sum (6 - s)k_s = 0$$

where k_s is the number of rings having n sides [44]. The equation describes how the curvature introduced by smaller rings is compensated by inverse curvature introduced by larger rings. A sum which deviates from zero indicates a deformation of the flat 2D structure. Crystalline structures, with only six-membered rings, easily fulfill the requirement. Considering the counts from figure 1(b) for domain boundaries gives a sum of − 2, a small deviation given the large sample size. Amorphous 2D silica, from figure 1(c), also fulfills the requirement of Euler's theorem, with a sum of 0 [45].

To further clarify the relationship between amorphous domains, defected crystalline domains, and purely crystalline domains, silicon-silicon nearest neighbor directed distance orientations (DDOs) were considered for each case. The directed distance orientation is the angle of the connection line between two neighboring Si atoms with respect to the image abscissa and it provides a metric for the order of the system. It was previously reported that crystalline phase DDOs exhibit three distinct values while amorphous phase DDOs have no

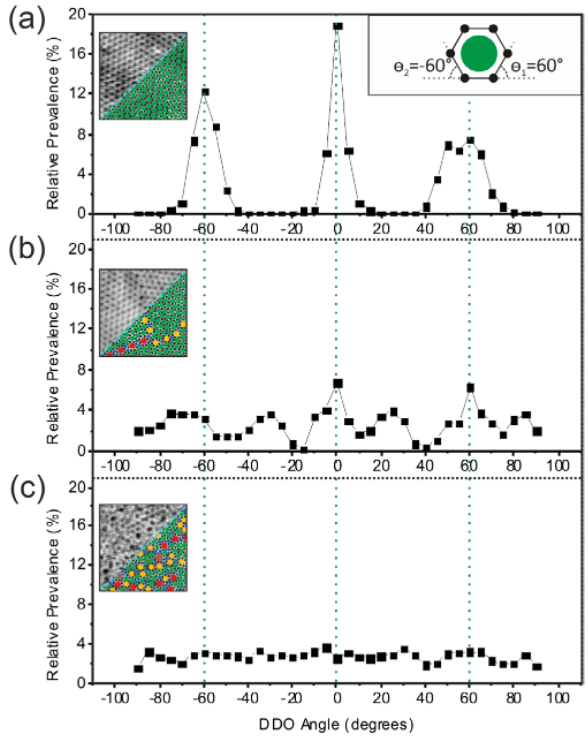

Figure 2. Distance directed orientations. Histograms of silicon–silicon nearest neighbor DDOS are shown for (a) purely crystalline silica, (b) crystalline silica with domain boundaries, and (c) amorphous silica. DDOs are derived by analyzing the images in figure 1, shown here as insets on the left-hand side of each plot. The inset in the right-hand corner of (a) shows a schematic diagram of the DDO angle assignment from the image abscissa, highlighting the origin of angles observed in the crystalline phase. Green dotted lines indicate the location of the peaks from the crystalline phase. All three plots are shown with the same vertical scale to facilitate direct comparisons of the relative prevalence of each angle between the distinct silica structures.

obvious preferential direction [46]. Figures 2(a) and (c) show histograms of the DDOs computed for the coordinates associated with the crystalline region in figure 1(a) and the amorphous region in figure 1(c), respectively. In the crystalline histogram, three peaks are observed at − 60 °, 0° and 60°, while in the amorphous histogram all values have approximately the same magnitude, confirming the earlier findings. Figure 2(b) shows a histogram of the DDOs for the crystalline region with domain boundaries shown in figure 1(b). In this case peaks at − 60 °, 0° and 60° mirror those observed in the crystalline phase. Additional peaks can be identified at − 30 ° and 30°, which are associated with a 30° rotated crystalline domain seen in the upper right corner of figure 1(b). A direct calculation of the DDOs specifically associated with the domain boundaries shows sets of multiple distinct values, depending on the boundary type. 57 boundaries exhibit a greater variety of DDOs than do 558 boundaries (boundary classifications are discussed in greater detail below). In both cases, there are more preferred directions than the three observed in the crystalline phase; unlike the amorphous phase, there is nonetheless a clear set of preferred values.

Ring statistics and DDOs provide mixed evidence as to whether the three structures shown in figure 1 may be thought of as distinct systems or, rather, as a continuous transition of the same system with domain boundaries comprising an increasingly large percentage of the film structure. To further explore this question, we now turn to a more detailed discussion of particular boundary structures and defects.

4. Domain boundaries and defect structures

The particular domain boundaries and defect structures that have been observed for bilayer silica on Ru(0001) include rotational boundaries, antiphase boundaries, closed loop boundaries, and complex boundaries. Dauphiné twin boundaries, which have been found to be composed of 6-membered rings in studies of bulk α-quartz [31, 47], have not been observed in silica bilayer films on ruthenium. For the purposes of comparing the boundaries in bilayer silica films to amorphous silica structures, we classify the boundaries based on their ring statistics: 57 boundaries, 558 boundaries, and complex boundaries.

4.1. 57 boundaries

One type of boundary commonly observed is the 57 boundary, composed of alternating pentagons and heptagons, as shown in figure 3(a). 57 type boundaries are rotational domain boundaries and the boundary itself exhibits a meandering path. The crystalline domains on either side of these boundaries have lattices that are rotated by 30° with respect to each other. Similar boundaries have been observed in graphene and in silica bilayer films grown on graphene [15, 23, 48]. Calculations of the strain fields and formation energy by density functional theory from those studies indicate the energetic favorability of defects involving rotations (such as the 57 defects shown here).

Here, we consider the relationship between the domains on either side of the 57 boundary and the underlying Ru(0001) substrate. DFT, STM, and LEED indicate that crystalline silica films preferentially grow with the underlying Ru(0001) substrate orientation [37]. A model showing the relationship between the silica structure with the 57 boundary and the underlying substrate is shown in figure 4(a); here, silica film position assignments above the substrate on the left-hand side of the boundary are based on published DFT results [37]. Domains with 30° rotation from the energetically preferred orientation exhibit a commensurate structure with the Ru(0001) substrate; this is highlighted in figure 4(a) with black dashed-line circles indicating ring centers in the rotated phase on the right-hand side of the figure which are situated over the same substrate lattice positions (e.g. the hollow site) as all ring centers from the domain on the left-hand side. Sharp reflexes in LEED diffraction indicate that for crystalline preparations the silica orientation is in registry with the substrate orientation [37]. Based on this and STM observations of crystalline domain orientations in which the rotated phase accounts for less than 8% of the crystalline area, we conclude that the 30° rotated commensurate structure represents

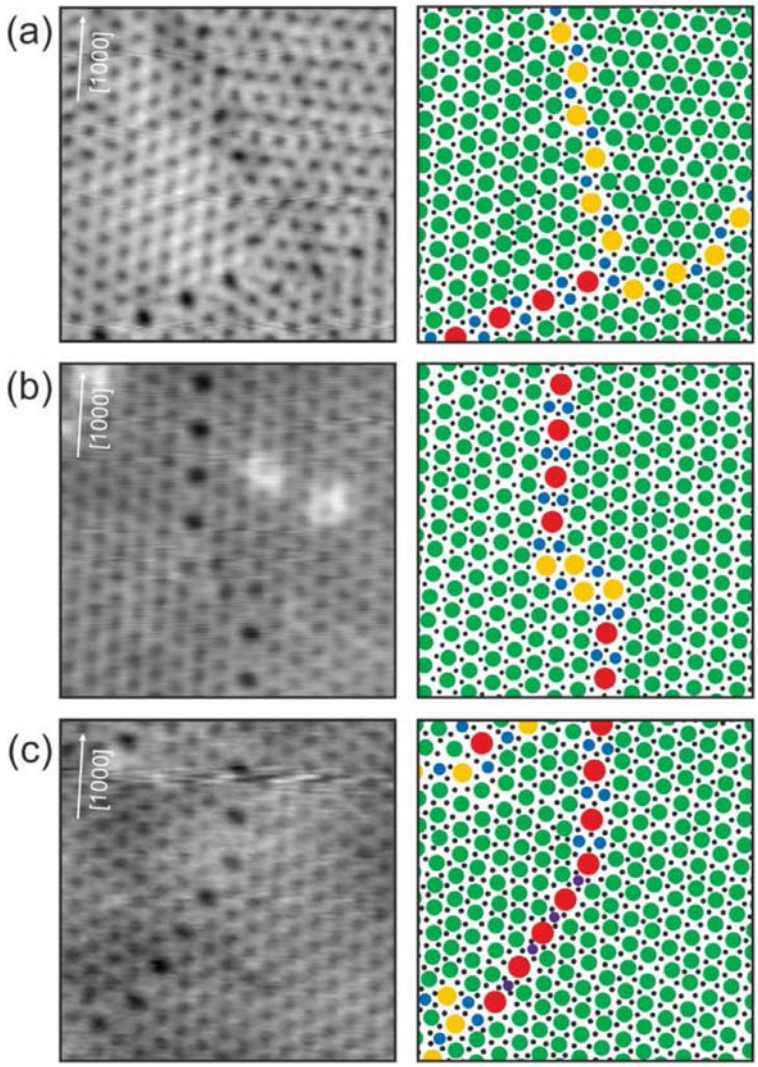

Figure 3. Common domain boundaries. STM images showing (a) two segments of a 57 boundary and a short segment of a 558 boundary (I_T = 100 pA, V_S = 0.5 V, scan area = 7.4 nm × 7.4 nm), (b) two 558 boundary segments connected by a group of five- and seven-membered rings (I_T = 10 pA, V_S = 2.0 V, scan area = 7.4 nm × 7.4 nm), and (c) a complex boundary, consisting in different portions of 57, 558, and 48 boundary sections (I_T = 100 pA, V_S = 1.0 V, scan area = 7.4 nm × 7.4 nm). For each image, diagrams are shown in the right-hand column which display the silicon atomic positions (black dots) and rings sizes and positions (colored circles, color-coded as in figure 1).

a minority of the crystalline silica domains in the silica bilayer. This conclusion is further supported by the relative prevalence of the 57 domain boundary in the silica bilayer. Although the 57 boundary is common, the 57 line defect is not observed as often as the 558 boundary, an antiphase boundary which separates two regions, each with substrate registry (see section 4.2). 29 domain boundary segments consisting of at least three 57 or 558 units were identified and analyzed. From this analysis, it was found that 558 boundaries account for approximately 55% of boundaries in terms of number of boundaries identified and approximately 65% when length is taken into account. The relative prevalence of particular domain boundary structures may relate to an energetic preference for registry between the ruthenium substrate and the bilayer silica film [37]. We now turn to a discussion of the ring combinations for the 57 boundaries. The tendency for boundaries with equivalent numbers of five- and seven-membered rings to form is consistent with the geometric constraints imposed by the two-dimensionality of the system. The 57 boundary fulfills the ring-size population requirement for closed 2D planar structures from Euler's theorem, because curvature induced by the five-membered rings is compensated by the seven-membered rings which contribute inverse curvature of the same absolute value, resulting in a total sum of zero. A sum which deviates from zero indicates a deformation of the flat 2D structure. Amorphous 2D silica comparably fulfills the requirement of Euler's theorem [45]. The ring neighborhoods introduced in 57 domain boundaries can be compared with

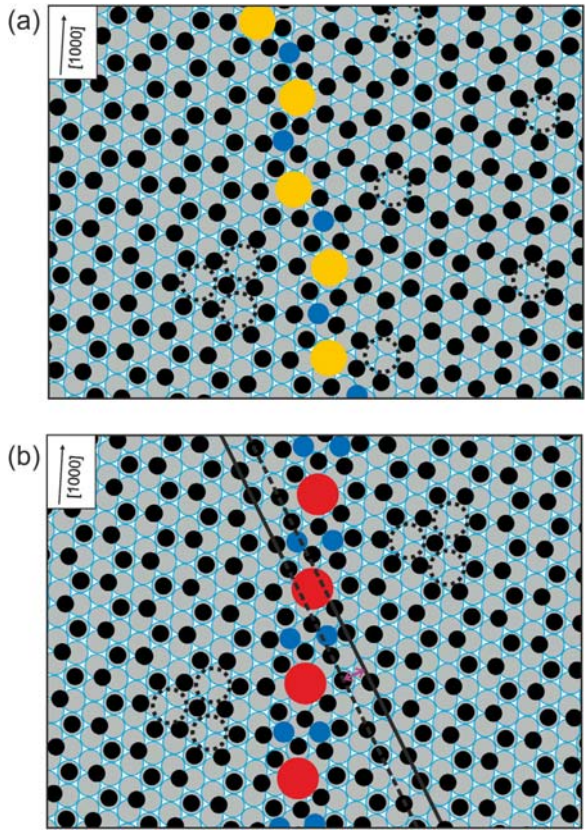

Figure 4. Domain boundaries and the Ru(0001) substrate. Diagrams detailing a possible relationship between silica films with domain boundaries and the Ru(0001) substrate for (a) a 57 boundary and (b) a 558 boundary. Blue circles indicate ruthenium atoms, black dots indicate silicon positions, and colored circles indicate the location of the boundary and its ring sizes (color-coded as in figure 1). In (a) black dashed-line circles demonstrate silica rings which sit over identical hollow sites in the substrate, highlighting the commensurate structure of the rotated silica phase on the right-hand side of the image with the Ru(0001) substrate and the registry between silica and Ru(0001) on the left-hand side. In (b) black lines and a purple arrow highlight the offset between the two crystalline domains that results from the antiphase boundary.

those present in the amorphous phase. Büchner *et al* characterized the prevalence of particular ring combinations observed in high-resolution STM images of amorphous silica bilayers by considering ring triplets. Ring triplets are sets of three adjacent rings which share a central silicon atom [33]. That study found that 567 ring triplets occur most frequently, followed by 667 triplets and 566 triplets. The 57 domain boundary is composed exclusively of these common ring triplets. Thus, regarding the ring combinations, 57 domain boundaries exhibit a number of similarities to the amorphous phase.

Pair distance histograms (PDHs) can be used to determine characteristic distances for short-, medium-, and long-range order. For example, PDHs for pairs of ring-center positions in amorphous silica exhibit several discernable peaks in 0–2 nm range, associated with nearest-neighbor and next-nearest-neighbor ring distances [49]. Using STM images of 57 domain boundaries, 558 domain boundaries, and the amorphous network, ring center positions were determined and ring-center pair distances subsequently calculated for each individual ring size. Raw pair distance counts are normalized by $\frac{1}{r[N_p]}$ where r is the radial distance and N_p is the total number of n-membered ring pair counts. This normalization corrects for increasing counts with distance and facilitates comparison of peak positions between differently sized data sets for the n-membered ring PDHs (e.g. due to ring statistics there are more 6-membered rings than 5-membered rings for a given image of the amorphous phase). The same normalization scheme is used for the domain boundary PDH plots for consistency. The normalized PDHs for each ring size are shown in figure 5. The peaks in the PDH plots reveal the spatial distribution of rings sizes. They give, for example, the characteristic distances between two five-membered rings within the amorphous bilayer silica structure.

First, we will discuss PDHs of ring center positions for 57 boundaries (figure 5(a)) in comparison with PDHs for individual ring sizes in the amorphous phase in figure 5(c). The magnitude of the normalized intensity for peaks in the domain boundary plots is higher than for comparable peak positions in the amorphous plots, indicating that the relative probability of finding a ring at that distance with respect to a reference ring is higher within domain boundary structures. Distinctions between domain boundaries and amorphous structures are also evident from peak positions. The first two peaks for the five-membered rings the amorphous silica plots are situated at radial distances of approximately 0.4 nm and 0.8 nm (this is indicated by blue dashed lines in figure 5). Larger ring sizes show peaks at increasingly larger distances. Beyond 1.7 nm, peaks for all individual ring size amorphous distributions become more difficult to discern, indicating a lack of longer range order in the amorphous structure. Figure 5(a) shows the PDHs for five- and seven-membered rings within the 57 boundary structure. For both five- and seven-membered rings, the first peak is positioned at approximately 1 nm; this corresponds with the third peak in the amorphous PDH for five-membered rings and the second peak in the amorphous PDH for seven-membered rings. Because each seven-membered ring is separated by a five-membered ring from the next seven-membered ring, the characteristic 'nearest-neighbor' distance associated with the first peak the amorphous PDHs is missing in the domain boundary structure. Furthermore, the structure of the 57 domain boundary enforces comparable peak distances for both the five- and seven-membered rings in contrast to the increasing distances observed in the amorphous phase. Finally, it should be noted that peaks from the 57 domain boundary can be clearly distinguished even at distances beyond 1.7 nm due to the patterned structure of the domain boundaries. Thus, comparing PDHs shows a level of order within domain boundary structures that is absent in the amorphous phase.

4.1.1. Closed-loop 57 boundaries. The most common clusters and point defects which we observed in the silica bilayer structure are displayed in figure 6. Each of these defects

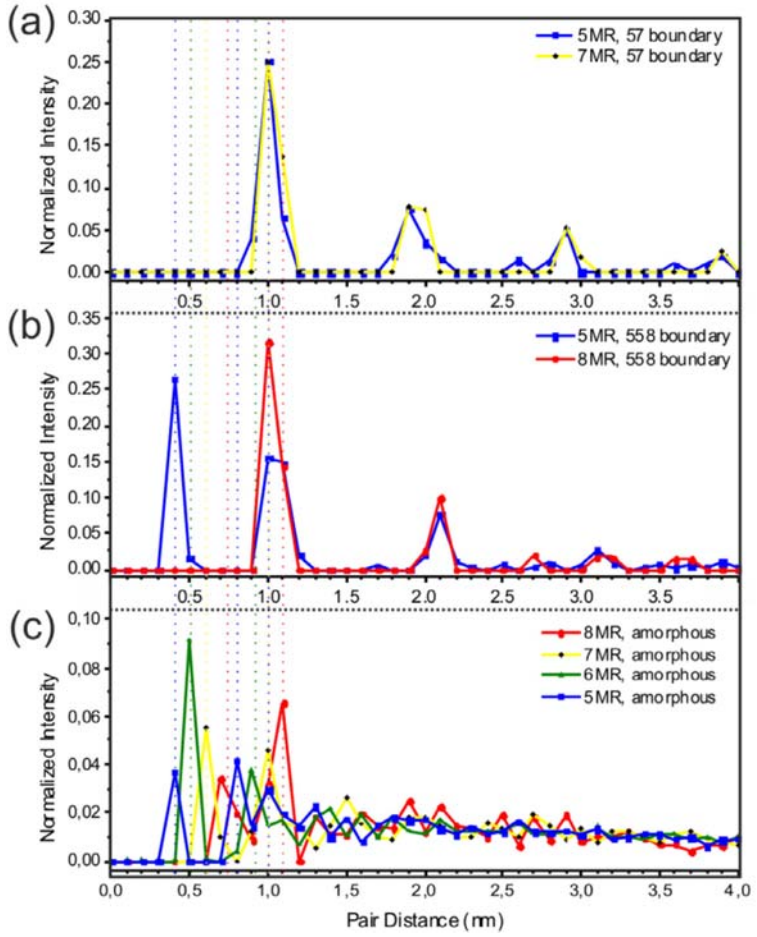

Figure 5. Pair distance histograms. Normalized pair distance histograms, showing the characteristic distances between the center positions of rings of the same size, are plotted for (a) 57 domain boundaries, (b) 558 domain boundaries, and (c) the amorphous silica phase. Dotted lines show the positions of the first peaks for each ring size from the pair distance histograms of the amorphous phase.

consists of five-, six-, and seven-membered rings with equal numbers of five- and seven-membered rings. The defects are a special, closed loop domain boundary case of the 57 domain boundaries. In the case of the flower (figure 6(a)), the boundary encompasses a small, seven-atom crystalline domain. In the case of the cross (figure 6(b)) it encompasses a two-atom crystalline domain. Like the domains separated by 1D meandering 57 domain boundaries, the domains encompassed by the closed loop domain boundaries exhibit a 30° lattice rotation with respect to the surrounding crystalline lattice. For the Stone–Wales defect in figure 6(c) [50], a second crystalline domain is not present. Stone–Wales defects are quite common in other 2D materials, such as graphene [18, 51, 52]. Larger closed-loop boundaries are also observed in graphene [15, 53]. In silica, the special closed-loop case of the 57 domain boundary maintains the similarities to the ring triplets in the amorphous phase, however the high symmetry observed for these clusters is different from what is observed in the amorphous phase.

4.2. 558 boundaries

The most prevalent of the boundaries observed is the 558 antiphase boundary, an example of which is shown in figure 3(b). Unlike the meandering 57 boundaries, 558 boundaries are straight, exhibiting a single orientation for any given domain boundary. Figure 3(b) shows two sections of 558 with the same orientation but an offset in lateral position. In this case, the offset is bridged by a pair of five- and seven-membered rings. In general, we observe that changes in the orientation or lateral position of the 558 type boundaries are connected by rings of other sizes. 558 boundaries exhibit preferential orientations with respect to the Ru substrate lattice vectors. Specifically, the observed orientations mirror the three-fold symmetry of the Ru(0 0 0 1) substrate with orientation angles of approximately 0, 60, and 120 degrees from the [1 0 0 0] direction of the underlying Ru substrate, suggesting that the Ru substrate plays a role in templating the 558 boundary.

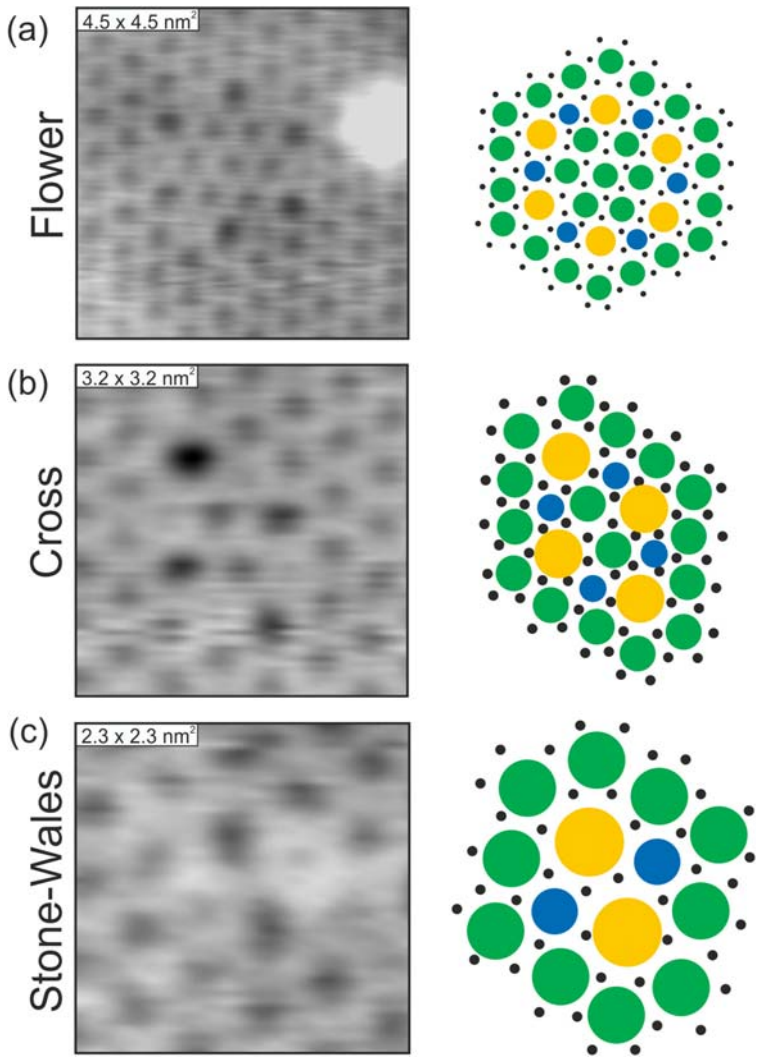

Figure 6. Common defect structures. STM images of common defect structures in bilayer silica with models showing their ring size distributions, each a special closed-loop case of a 57 boundary: (a) flower (I_T = 100 pA, V_S = 3.0 V), (b) cross (I_T = 100 pA, V_S = 2.0 V), and (c) Stone–Wales defect (I_T = 100 pA, V_S = 1.0 V).

A structural model incorporating DFT results from the purely crystalline silica films [37] and from the empirically observed domain boundary structure was developed to examine the structural relationship between the silica film boundary structure and that of the Ru substrate (figure 4(b)). DFT indicates that for silica films grown in an oxygen-rich atmosphere, as is the case for the samples in this study, a configuration with Si atoms situated above hollow sites and atop sites of the Ru is energetically favorable [37]. Measurements of the crystalline lattice offset between domains, domain boundary width, and domain boundary atomic positions were established from STM images; the boundary width of the 558 boundary is 2.2 times the lattice constant of the silica lattice. An idealized structural model incorporating these empirical values was developed for the silica film model. Overlaying this structural model of silica on the model of the Ru substrate in the energetically favorable configuration reveals that crystalline domains on either side of the boundary show an equivalent relationship with the underlying substrate, offset by a single Ru(0 0 0 1) atomic position in the [1 1 0 0] direction (as shown by the purple double headed arrow in figure 4(b)). The experimentally observed ovular shape of the eight-membered rings is reproduced by the model. Furthermore, the model is consistent with the observed orientation with respect to the substrate. This points to the important role that the substrate plays for this particular type of boundary.

The importance of the substrate is substantiated by considering the literature for domain boundaries in bilayer silica grown on graphene, Pd(0 0 1) and Pt(1 1 1) overviewed in table 1. The 558 boundary structure in silica bilayers appears to be unique to the Ru(0 0 0 1) substrate, as such a boundary in silica has not, to our knowledge, been reported for bilayer silica films on other substrates (see table 1). Another antiphase boundary has been observed in bilayer silica grown on on

Pd(0 0 1) [24]. However, the structure of that boundary, composed entirely of elongated eight-membered rings, is quite different from the 558 antiphase boundary on Ru(0 0 0 1). Altman *et al* [24] proposed that the elongated eight-membered ring domain boundary arose due to defect structures between the silica planes which help relieve the tensile stress in the bilayer. DFT and spectroscopy measurements indicate that the silica bilayer structure on Ru(0 0 0 1) is composed of Si–O–Si bridges perpendicular to the substrate [37], such that the structure of the 1D defects observed in this study are expected to be mirrored in both the vacuum exposed side of the film and the substrate facing layer. The structural differences point to the role that substrate plays in the development of domain boundaries.

We now turn to a discussion of ring combinations specific to the 558 domain boundary. Comparing the 558 boundary to the amorphous phase shows that the similarities between this boundary and the amorphous phase are weaker than for the 57 boundary. For the 558 boundary, triplet combinations of 566, 568, 668, and 558 are observed. According to Büchner *et al*, these are the third, fourth, seventh, and eighth most prevalent combinations in the amorphous phase [33]. Thus the ring triplets involved in this boundary are observed less often in the amorphous phase than those of the 57 boundary.

PDHs, shown in figure 5(b), also reveal differences between the 558 boundary structures and the amorphous bilayer silica structure. Like the 57 boundary structures, peaks can clearly be distinguished at longer distances than for the amorphous structure due to the regular patterned structure of the domain boundaries. Five-membered ring PDHs from the 558 boundary exhibit peaks that correspond to the first and third peaks of the five-membered ring amorphous PDH. The first peak, associated with nearest-neighbors shows strong agreement—this is simply the distance between the centers of two neighboring five-membered rings. The next peak in the five-membered ring PDH from the 558 boundary is at a larger distance than the next peaks in the amorphous phase. This can also be easily understood by considering the large area of the eight-membered ring which separates pairs of five-membered rings in the 558 boundary. Within the amorphous phases a variety of ring sizes may separate five-membered rings, leading to a smaller distance between two next-nearest neighbor five-membered rings on average. Similar reasoning is easily applied to understand the position of the first eight-membered ring peak in the 558 PDH with respect to the second peak in the amorphous phase—the small size of the five-membered ring gives rise to shorter distances. Additionally, a peak is not observed at 0.74 nm because within the 558 boundary, eight-membered rings never have another eight-membered ring as the nearest-neighbor. It should be noted that the 558 boundary does satisfy Euler's theorem as required for flat 2D surfaces. Taken together, the ring combinations and pair distance histograms indicate that 558 boundaries are quite distinct from amorphous phase structures.

4.3. Complex boundaries

More complex boundaries are also observed. These boundaries are characterized by combinations of several distinct boundary types or by irregular arrangements of different ring sizes with limited periodicity separating two crystalline domains. The boundary in figure 3(c) is one example of a complex boundary. It presents a meandering 57 configuration in the bottom left of the image, transitions into a straight boundary of eight- and four-membered rings, and then displays a second transition to a 558 boundary in the top right. Like the more prevalent 57 and 558 boundaries, the 48 segment of this boundary also satisfies Euler's theorem as required for a flat film structure in 2D space. Strain introduced by larger rings is compensated for by the presence of small rings; in this case a four-membered ring compensates each 8-membered ring. Like the 558 segments, the 48 segment shown here is straight and the crystalline domains maintain their orientation angle across the boundary. 48 segments are rarely observed; the segments tend to be short and are often combined with other ring structures, as seen in figure 3(c). Complex boundaries like this, though less commonly observed than the 57 and 558 boundaries, point to the rich variety of domain boundary structures present in the crystalline silica bilayer films.

5. Domain boundaries and the crystalline to amorphous transition

Identification of domain boundary structures gives insight into the relationship between purely crystalline, crystalline with domain boundaries and defects, and amorphous films. Whether these phases represent distinct systems or a continuous transition of the same system with domain boundaries comprising an ever larger percentage of the film structure can be assessed by considering spatial distributions of rings across a crystalline-amorphous interface in comparison with domain boundary structures. Studies of the ring statistics across a lateral transition between crystalline and amorphous regions of the bilayer silica have shown that this transition is continuous [36, 45]. In moving from crystalline to amorphous regimes, five- and seven-membered rings are introduced first while four-, eight-, and nine-membered rings appear later in the transition. In this case four-, eight-, and nine-membered rings are not directly interfaced with the crystalline phase. In contrast, the ring statistics for domain boundaries and defect structures represent point and line defects that are directly interfaced with crystalline phases of silica; the boundary is discrete, not continuous. Here, we see that both eight- and four-membered rings are in direct contact with the crystalline domain in the form of 558 and 48 boundaries, a configuration which is not observed in the continuous transition between crystalline and amorphous regions of the silica bilayer. 57 boundaries show greater consistency with the previously reported characterization of the crystalline to amorphous transition region, however in this case there is periodicity in the arrangement of the five- and seven-membered rings while in the transition region five- and seven-membered rings are interspersed with six-membered rings.

6. Summary

We have presented a study of the most common domain boundaries in bilayer silica on Ru(0 0 0 1). The domain boundaries

were considered in the context of their relationship to amorphous silica structures. By using real space atomic position data from chemically equivalent and well-defined systems, the structural similarities between domain boundary structures and amorphous structures were assessed directly. Ring statistics, ring neighborhoods DDOs, and PDHs provide metrics to describe the similarities and differences between purely crystalline, crystalline with domain boundaries and defects, and amorphous films. The results show that similarities between domain boundaries and amorphous phases may depend critically on which type of domain boundary is being considered. 57 boundaries exhibit stronger similarities to the amorphous phase than 558 boundaries as seen by considerations of ring neighborhoods, ring statistics across amorphous-crystalline interfaces, and the greater variety of DDOs that arise from the 57 boundaries. Nonetheless, both 558 and 57 boundaries exhibit a degree of order and periodicity that is lacking in the amorphous phase, as evidenced by differences in ring-center pair distance histograms for individual ring sizes. From this we conclude that, contrary to the predictions of cybotactic groupings or Rosenhain's amorphous cement model, the particular domain boundaries observed in this study are distinct from the glassy state.

While 2D model systems present well-defined structures ideal for surface science characterization, in generalizing the results to bulk structures the role of the substrate must also be considered. The formation of domain boundaries depends on energetics, strain, and substrate interactions. 57 boundaries are seen in a variety of 2D materials as well as in the silica bilayer films on other substrates, while the 558 boundary in silica appears to be unique to the preparation on Ru(0001). Because the presence of domain boundaries can have an important effect on material properties, an ability to control for the prevalence and type domain boundary structures is desirable. Domain boundary engineering takes advantage of the dramatically different physical and chemical properties inside boundaries and interfaces, as compared to the bulk, for the development of new technologies [22]. The use of different substrate materials (or composite materials) with unique lattice constants and chemical interactions may offer new routes towards tailoring ring size distributions in 2D materials for optimized chemical, mechanical, and electronic performance.

Acknowledgments

The authors would like to thank Leonid Lichtenstein for helpful discussions. KMB gratefully acknowledges the support of the Alexander von Humboldt foundation. CB is grateful to the CRC 1109, funded by the Deutsche Forschungsgemeinschaft for financial support.

References

[1] Wright A C 1994 Neutron scattering from vitreous silica. V. The structure of vitreous silica: what have we learned from 60 years of diffraction studies? *J. Non-Cryst. Solids* 179 84–115

[2] Wright A C 2014 The great crystallite versus random network controversy: a personal perspective *Int. J. Appl. Glass Sci.* 5 31–56

[3] Stewart G W 1930 X-ray diffraction in liquids *Rev. Mod. Phys.* 2 116–22

[4] Valenkov N and Poray-Koshitz E 2015 X-ray investigation of the glassy state *Z. Für Krist.—Cryst. Mater.* 95 195–229

[5] Rosenhain W and Ewen D 1913 The intercrystalline cohesion of metals *J. Inst. Met.* 10 119–49

[6] Zhang H, Srolovitz D J, Douglas J F and Warren J A 2009 Grain boundaries exhibit the dynamics of glass-forming liquids *Proc. Natl Acad. Sci. USA* 106 7735–40

[7] Keblinski P, Phillpot S R, Wolf D and Gleiter H 1997 Amorphous structure of grain boundaries and grain junctions in nanocrystalline silicon by molecular-dynamics simulation *Acta Mater.* 45 987–98

[8] Ainslie N G, Mackenzie J D and Turnbull D 1961 Melting kinetics of quartz and cristobalite *J. Phys. Chem.* 65 1718–24

[9] Gong W L, Wang L M, Ewing R C and Fei Y 1996 Surface and grain-boundary amorphization: thermodynamic melting of coesite below the glass transition temperature *Phys. Rev.* B 53 2155–8

[10] Yazyev O V and Louie S G 2010 Topological defects in graphene: dislocations and grain boundaries *Phys. Rev.* B 81 195420

[11] Yazyev O V and Louie S G 2010 Electronic transport in polycrystalline graphene *Nat. Mater.* 9 806–9

[12] Grantab R, Shenoy V B and Ruoff R S 2010 Anomalous strength characteristics of tilt grain boundaries in graphene *Science* 330 946–8

[13] Huang P Y *et al* 2011 Grains and grain boundaries in single-layer graphene atomic patchwork quilts *Nature* 469 389–92

[14] Lahiri J, Lin Y, Bozkurt P, Oleynik I I and Batzill M 2010 An extended defect in graphene as a metallic wire *Nat. Nanotechnol.* 5 326–9

[15] Cockayne E, Rutter G M, Guisinger N P, Crain J N, First P N and Stroscio J A 2011 Grain boundary loops in graphene *Phys. Rev.* B 83 195425

[16] Ago H, Fukamachi S, Endo H, Solís-Fernández P, Mohamad Yunus R, Uchida Y, Panchal V, Kazakova O and Tsuji M 2016 Visualization of grain structure and boundaries of polycrystalline graphene and two-dimensional materials by epitaxial growth of transition metal dichalcogenides *ACS Nano* 10 3233–40

[17] Zhang Z, Yang Y and Yakobson B I 2014 Grain boundaries in hybrid two-dimensional materials *J. Mech. Phys. Solids* 70 62–70

[18] Yazyev O V and Chen Y P 2014 Polycrystalline graphene and other two-dimensional materials *Nat. Nanotechnol.* 9 755–67

[19] Büchner C, Lichtenstein L, Stuckenholz S, Heyde M, Ringleb F, Sterrer M, Kaden W E, Giordano L, Pacchioni G and Freund H-J 2014 Adsorption of Au and Pd on ruthenium-supported bilayer silica *J. Phys. Chem.* C 118 20959–69

[20] Ulrich S, Nilius N, Freund H-J, Martinez U, Giordano L and Pacchioni G 2008 Evidence for a size-selective adsorption mechanism on oxide surfaces: Pd and Au atoms on SiO_2/Mo(1 1 2) *ChemPhysChem* 9 1367–70

[21] Ulrich S, Nilius N, Freund H-J, Martinez U, Giordano L and Pacchioni G 2009 Realization of an atomic sieve: silica on Mo(1 1 2) *Surf. Sci.* 603 1145–9

[22] Salje E K H 2010 Multiferroic domain boundaries as active memory devices: trajectories towards domain boundary engineering *ChemPhysChem* 11 940–50

[23] Bjorkman T, Kurasch S, Lehtinen O, Kotakoski J, Yazyev O V, Srivastava A, Skakalova V, Smet J H, Kaiser U and Krasheninnikov A V 2013 Defects in bilayer silica and

graphene: common trends in diverse hexagonal two-dimensional systems *Sci. Rep.* 3 3482
[24] Altman E I, Götzen J, Samudrala N and Schwarz U D 2013 Growth and characterization of crystalline silica films on Pd(1 0 0) *J. Phys. Chem.* C 117 26144–55
[25] Yu X, Yang B, Boscoboinik J A, Shaikhutdinov S and Freund H-J 2012 Support effects on the atomic structure of ultrathin silica films on metals *Appl. Phys. Lett.* 100 151608
[26] Kundu M and Murata Y 2002 Growth of single-crystal SiO_2 film on Ni(1 1 1) surface *Appl. Phys. Lett.* 80 1921–3
[27] Boscoboinik J A, Yu X, Yang B, Shaikhutdinov S and Freund H-J 2013 Building blocks of zeolites on an aluminosilicate ultra-thin film *Microporous Mesoporous Mater.* 165 158–62
[28] Weissenrieder J, Kaya S, Lu J-L, Gao H-J, Shaikhutdinov S, Freund H-J, Sierka M, Todorova T K and Sauer J 2005 Atomic structure of a thin silica film on a Mo(112) substrate: a two-dimensional network of SiO_4 tetrahedra *Phys. Rev. Lett.* 95 76103
[29] Mathur S, Vlaic S, Machado-Charry E, Vu A-D, Guisset V, David P, Hadji E, Pochet P and Coraux J 2015 Degenerate epitaxy-driven defects in monolayer silicon oxide on ruthenium *Phys. Rev.* B 92 161410
[30] Yang B, Boscoboinik J A, Yu X, Shaikhutdinov S and Freund H-J 2013 Patterned defect structures predicted for graphene are observed on single-layer silica films *Nano Lett.* 13 4422–7
[31] Eder S D, Fladischer K, Yeandel S R, Lelarge A, Parker S C, Søndergård E and Holst B 2015 A giant reconstruction of α-quartz (0 0 0 1) Interpreted as three domains of nano dauphine twins *Sci. Rep.* 5 14545
[32] Lichtenstein L, Buechner C, Yang B, Shaikhutdinov S, Heyde M, Sierka M, Wlodarczyk R, Sauer J and Freund H-J 2012 The atomic structure of a metal-supported vitreous thin silica film *Angew. Chem., Int. Ed.* 51 404–7
[33] Büchner C, Liu L, Stuckenholz S, Burson K M, Lichtenstein L, Heyde M, Gao H-J and Freund H-J 2016 Building block analysis of 2D amorphous networks reveals medium range correlation *J. Non-Cryst. Solids* 435 40–7
[34] Huang P Y, Kurasch S, Alden J S, Shekhawat A, Alemi A A, McEuen P L, Sethna J P, Kaiser U and Muller D A 2013 Imaging atomic rearrangements in two-dimensional silica glass: watching silica's dance *Science* 342 224–7
[35] Huang P Y *et al* 2012 Direct imaging of a two-dimensional silica glass on graphene *Nano Lett.* 12 1081–6
[36] Lichtenstein L, Heyde M and Freund H-J 2012 Crystalline-vitreous interface in two dimensional silica *Phys. Rev. Lett.* 109 106101
[37] Loeffler D *et al* 2010 Growth and structure of crystalline silica sheet on Ru(0 0 0 1) *Phys. Rev. Lett.* 105 146104
[38] Yang B *et al* 2012 Thin silica films on Ru(0 0 0 1): monolayer, bilayer and three-dimensional networks of SiO_4 tetrahedra *Phys. Chem. Chem. Phys.* 14 11344–51
[39] Rust H-P, Heyde M and Freund H-J 2006 Signal electronics for an atomic force microscope equipped with a double quartz tuning fork sensor *Rev. Sci. Instrum.* 77 43710
[40] Heyde M, Simon G H, Rust H-P and Freund H-J 2006 Probing adsorption sites on thin oxide films by dynamic force microscopy *Appl. Phys. Lett.* 89 263107
[41] Kumar A, Sherrington D, Wilson M and Thorpe M F 2014 Ring statistics of silica bilayers *J. Phys.: Condens. Matter* 26 135401
[42] Shackelford J F and Brown B D 1981 The lognormal distribution in the random network structure *J. Non-Cryst. Solids* 44 379–82
[43] Buechner C, Schlexer P, Lichtenstein L, Stuckenholz S, Heyde M and Freund H-J 2014 Topological investigation of two-dimensional amorphous materials *Z. Phys. Chem.—Int. J. Res.* 228 587–607
[44] Ebbesen T W 1998 Cones and tubes: geometry in the chemistry of carbon *Acc. Chem. Res.* 31 558–66
[45] Burson K M, Schlexer P, Büchner C, Lichtenstein L, Heyde M and Freund H-J 2015 Characterizing crystalline-vitreous structures: from atomically resolved silica to macroscopic bubble rafts *J. Chem. Educ.* 92 1896–902
[46] Lichtenstein L, Heyde M and Freund H-J 2012 Atomic arrangement in two-dimensional silica: from crystalline to vitreous structures *J. Phys. Chem.* C 116 20426–32
[47] Calleja M, Dove M T and Salje E K H 2001 Anisotropic ionic transport in quartz: the effect of twin boundaries *J. Phys.: Condens. Matter* 13 9445
[48] Banhart F, Kotakoski J and Krasheninnikov A V 2011 Structural defects in graphene *ACS Nano* 5 26–41
[49] Burson K M, Gura L, Kell B, Büchner C, Lewandowski A L, Heyde M and Freund H-J 2016 Resolving amorphous solid–liquid interfaces by atomic force microscopy *Appl. Phys. Lett.* 108 201602
[50] Stone A J and Wales D J 1986 Theoretical studies of icosahedral C60 and some related species *Chem. Phys. Lett.* 128 501–3
[51] Ma J, Alfè D, Michaelides A and Wang E 2009 Stone–Wales defects in graphene and other planar sp^2-bonded materials *Phys. Rev.* B 80 33407
[52] Kotakoski J, Krasheninnikov A V, Kaiser U and Meyer J C 2011 From point defects in graphene to two-dimensional amorphous carbon *Phys. Rev. Lett.* 106 105505
[53] Gong C, He K, Chen Q, Robertson A W and Warner J H 2016 *In situ* high temperature atomic level studies of large closed grain boundary loops in graphene *ACS Nano* 10 9165–73